Pole-to-pole vertical ionospheric profiles at Jupiter from JWST

JGR Space Physics

RESEARCH ARTICLE
10.1029/2025JA034066

Pole-to-Pole Vertical Ionospheric Profiles at Jupiter From JWST

Paola I. Tiranti[1], H. Melin[1], L. Moore[2], K. L. Knowles[1], T. S. Stallard[1], J. O'Donoghue[3], K. Roberts[2], K. Mohamed[2], and E. M. Thomas[1]

[1]Northumbria University, Newcastle, UK, [2]Boston University, Boston, MA, USA, [3]University of Reading, Reading, UK

Key Points:

- Pole-to-pole H_3^+ vertical profiles show near constant temperature in altitude, with localized auroral heating of ~1900 K at 1,000 km altitude at the poles
- Vertical H_3^+ volumetric number density profiles show altitudinal variability, with multiple high altitude peaks
- H_3^+ vertical dawn densities at non-auroral latitudes are more than twice as large as dusk densities

Supporting Information:

Supporting Information may be found in the online version of this article.

Correspondence to:

P. I. Tiranti,
p.tiranti@northumbria.ac.uk

Citation:

Tiranti, P. I., Melin, H., Moore, L., Knowles, K. L., Stallard, T. S., O'Donoghue, J., et al. (2025). Pole-to-pole vertical ionospheric profiles at Jupiter from JWST. *Journal of Geophysical Research: Space Physics*, *130*, e2025JA034066. https://doi.org/10.1029/2025JA034066

Received 10 APR 2025
Accepted 12 AUG 2025

Abstract We present the first pole-to-pole observations of Jupiter's ionosphere, capturing dawn and dusk vertical structure up to 5,000 km altitude using the James Webb Space Telescope (JWST), simultaneous to Juno's radio occultation experiments (ROX) in September 2023. We produce vertical H_3^+ temperature global maps showing largely constant temperatures with altitude. Mean temperatures range from ~650 K at low latitudes to ~800 K at high latitudes. Auroral emissions were observed at the north and south pole, with northern temperature profiles showing signatures of localized heating (up to 1900 K) at low altitudes. Temperature-latitude gradients exhibit steeper slopes at dusk compared to dawn at all altitudes, particularly between 1,500 and 1,700 km. We also produce the first pole-to-pole vertical H_3^+ volumetric number density map, with auroral densities of up to 5×10^9 m^{-3} peaking near 1,500 km altitude. We find a dawn-dusk asymmetry at sub-auroral and equatorial latitudes, with higher densities at dawn (1×10^8 m^{-3}) compared to dusk (5×10^7 m^{-3}) between 1,500 and 1,700 km. While photochemical equilibrium (PCE) theory predicts higher densities at dusk, the presence of enhanced dawn densities implies that additional processes—such as particle precipitation and plasma transport, particularly at high and mid latitudes—play a significant role in shaping the ionospheric structure.

Plain Language Summary We used the James Webb Space Telescope (JWST) to observe Jupiter's upper atmosphere from pole to pole at both dawn and dusk, up to 5,000 km in altitude. We present maps of upper atmosphere temperatures and ion densities across the planet. Our results show that temperature remains mostly constant with altitude, though localized heating up to 1900 K was detected at low altitudes in the northern aurora. We also found that temperature changes more steeply with latitude at dusk than at dawn, particularly between 1,500 and 1,700 km altitude. For the first time, we mapped ion density from pole to pole. We found unexpected higher densities at dawn than at dusk, which challenges the expected behavior of the ionosphere. In particular, we found an enhancement at low latitudes, away from auroral regions. These results provide new insights into Jupiter's ionospheric structure and dynamics, suggesting that additional processes may be shaping the planet's upper atmosphere.

1. Introduction

Jupiter's charged particle ionosphere is an important region of the atmosphere, as it enables an understanding of the overall planetary energy balance and coupling with the magnetosphere. To better characterize magnetosphere-ionosphere (MI) interactions, it is important to identify relevant ionospheric parameters such as temperature and ion density. Emissions from the upper atmosphere, both in the ultraviolet (UV) and infrared (IR), are a response to energy injected into the system, either from the Sun or via magnetospheric processes (Badman et al., 2015). Vertical electron and ion profiles are crucial for advancing our understanding of MI coupling. Particularly, there are missing components still to be addressed, such as:

1. the lack of observed vertical ionospheric volumetric number densities, especially at low latitudes, which are important constraints for models;
2. likewise, the lack of measured vertical ionospheric temperatures at all latitudes and altitudes;
3. the redistribution of auroral energy as seen in global measurements of the latitudinal temperature gradient in three dimensions.

The ionosphere is created via ionization of the main gases (H, H_2 and He) by extreme EUV radiation and by particle impact, producing H^+, H_2^+ and He^+. H_2^+ then undergoes an exothermic reaction with the surrounding H_2, forming H_3^+ (Miller et al., 2006). By analyzing H_3^+ emission lines with spectroscopic techniques, it is possible to

determine properties of the ion, such as temperature, density and total emission rate (which is its cooling rate). Production of H_3^+ by solar EUV ionization acts planet-wide on the dayside, with production rates determined by the solar zenith angle (SZA), such that the highest EUV production rates are generally expected at the sub-solar point. On the other hand, production by particle precipitation leads to high concentrations of the ion at the magnetic poles, following auroral mechanisms at Jupiter (Johnson et al., 2018; Lam et al., 1997; O'Donoghue et al., 2021).

H_3^+ was first detected at Jupiter in 1988 (Drossart et al., 1989), and subsequently at Saturn, Uranus, and Neptune (Geballe et al., 1993; Melin et al., 2025; Trafton et al., 1993). For Jupiter, in particular, H_3^+ spectral and imaging observations of auroral regions have been studied for decades (Miller et al., 2020). While recent observations highlighted a lack of understanding of phenomena that cause aurorae (Kurth et al., 2018; Mauk et al., 2020; Sulaiman et al., 2022), extensive campaigns with both HST, Juno and James Webb Space Telescope (JWST) shed a light on auroral morphology; see Nichols et al. (2009); Nichols et al. (2017, 2025). Juno data have revealed complex field-aligned currents, large-scale electron density depletion, and intense wave-particle interactions that challenge traditional steady-state models. Electron density profiles derived from Juno Waves observations demonstrate that Jupiter's topside ionosphere is highly variable and organized by magnetic longitude, possibly due to anomalies in the internal magnetic field structure (Kurth et al., 2025). Further, observations of broadband electron precipitation and coincident whistler-mode waves suggest that stochastic wave-driven acceleration plays a key role in auroral processes (Kurth et al., 2018), while the structuring of auroral zones into distinct current regions indicates significant variability in magnetosphere-ionosphere coupling (Sulaiman et al., 2022). These findings underscore the need for further studies to fully characterize the processes governing Jupiter's aurorae.

Models of different complexities have attempted to explain the observed UV and IR emissions in the aurora and to produce corresponding vertical electron and ion density profiles. The UV emission brightness is primarily driven by flux of precipitating electrons, which excite H and H_2 in the auroral region, producing prompt emissions. H_3^+ IR emissions scale with density, which depends on the H_2 ionization rate, ion transport and chemistry, and whose emission intensity is strongly influenced by atmospheric temperature (Yelle & Miller, 2004). Modeling has revealed that H_3^+ is an essential component in the ionosphere at all altitudes, together with H^+ which prevails at higher altitudes and on the night side.

Waite Jr. et al. (1983) calculated the intensity of UV emissions resulting from the excitation generated by solar extreme UV (EUV) photons and auroral electrons, showing that precipitation alters the vertical temperature profile of the thermosphere, as well as the composition and structure of the ionosphere. Grodent et al. (2001) modeled the thermal response of Jupiter's upper atmosphere in response to electron precipitation and showed that the strongest UV volume emission was found to be 200 km above the 1-bar pressure level, lower than the altitude of the IR peak at 350 km. Hydrocarbons are found at low altitudes, and they have the ability to absorb UV radiation with wavelengths shorter than 140 nm. These hydrocarbons populate altitudes at and below the homopause, and H_3^+ cannot coexist due to its high reactivity. While H_3^+ is relatively stable in the upper atmosphere where only H, H_2, and He are present, it charge-exchanges rapidly with other species, such as CH_4, below the homopause. Additionally, rather than enhancing electron densities, hydrocarbons tend to minimize them, as their dissociative recombination rates are much faster than atomic loss processes and often exceed that of $H_3^+ + e^-$. This leads to the production of hydrocarbon molecular ions with short chemical lifetimes, replacing longer-lived H^+ and H_3^+ populations. H_3^+, which results from particle precipitation that deposits energy above the homopause, is efficiently destroyed at lower altitudes. Further, based on the color-ratio (which is the ratio between unabsorbed and hydrocarbon-absorbed UV intensity) and energy deposition features of auroral electrons, the electron energy at Jupiter was predicted to be in the range of 10s to a few 100s of keV (Gérard et al., 2002; Gustin et al., 2004).

The unexpectedly high temperatures at non-auroral latitudes observed in the upper atmospheres of all the giant planets cannot yet be fully explained by our understanding of available energy sources. On Earth, the upper atmosphere is primarily heated by solar EUV radiation (Rishbeth, 1988), but at the giant planets solar EUV provides <5% of the required energy (Koskinen et al., 2015; Yelle & Miller, 2004). This means that additional heat sources exist. Two main possibilities have been proposed: (a) Energy injected into the auroral regions at the magnetic poles may be redistributed across the planet (Brown et al., 2020; O'Donoghue & Stallard, 2022; Roberts et al., 2025). Models indicate that this transport is greatly inhibited by the strong Coriolis forces generated by the fast rotation of these planets (Smith & Aylward, 2009; Yates et al., 2020), and therefore determining temperature gradients would help in determining how efficient this redistribution is. (b) The turbulent lower atmosphere

generates gravity and/or acoustic waves that propagate upward and break in the upper atmosphere, releasing their energy (Barrow et al., 2012; Majeed et al., 2009; Matcheva & Strobel, 1999; Waite Jr. et al., 1983). Observations above the Great Red Spot at Jupiter, potentially a strong source of these waves, showed strong heating above this region (O'Donoghue et al., 2016), although at the same time, more recent observations revealed no significant heating (Melin et al., 2024; Roberts et al., 2025).

Ground-based campaigns have studied how H_3^+ varies across the disk of Jupiter, and the first global H_3^+ map was produced using the UK InfraRed Telescope (UKIRT). Lam et al. (1997) observed temperatures of 700 and 1000 K and H_3^+ column densities of $\sim 10^{16}$ m^{-2} in the auroral regions. At equatorial latitudes they observed temperature of 700–800 K, and H_3^+ column densities below 1×10^{15} m^{-2}. Keck II/NIRSPEC observations (O'Donoghue et al., 2021) produced high spatial resolution pole-to-pole temperature and density maps. These maps highlighted a steady gradient in temperature from hot auroral regions to cooler equatorial latitudes. This points to a redistribution of auroral energy being the predominant cause of upper atmospheric heating at low latitudes. H_3^+ emission measurements obtained with JWST, show a highly variable and diverse area around the Great Red Spot (GRS) region (Melin et al., 2024). The GRS was observed on 2022-7-27 at System III longitudes between 282.5°W and 303.8°W. Different features such as arcs, bands, and spots are seen above the anti-cyclone. This suggests that at low latitudes there must be a strong link between the lower and upper atmosphere, perhaps via gravity waves. These waves can drastically alter the local density structure, but appear to provide little heating. The small scale intricacies observed in this study revealed that the non-auroral ionosphere is more complex than previously thought, highlighting the need to further investigate the interplay between these heating mechanisms.

The vertical distribution of H_3^+ at Jupiter has been observed from both ground-based facilities and by *in situ* spacecraft. The first vertical profile, up to 3,500 km, was observed in the southern auroral region using Keck II/NIRSPEC spectrometer (Lystrup et al., 2008). For altitudes up to 1,800 km, ion densities are broadly consistent with models (Grodent et al., 2001). Exospheric temperatures were around 1450 K, which is 150 K higher than expected from Grodent et al. (2001). Subsequent observations with Subaru's InfraRed Camera and Spectrometer (IRCS) produced H_3^+ vertical emissivity profiles up to 3,000 km (Uno et al., 2014). The measurements focused on the H_3^+ overtone and hot overtones in the near-IR, finding that the peak altitudes for H_3^+ and hot overtones were 700–900 km and 680–950 km above the 1-bar level, respectively, which were lower than predicted by models (Grodent et al., 2001; Melin et al., 2005). Cassini/VIMS data from the 2000 to 2001 Jupiter flyby suggests that H_3^+ emission at mid-to-low latitudes originates between 300 and 500 km above the 1-bar level (Stallard et al., 2015) and is consistent with models (Tao et al., 2011). Observations with the GNIRS instrument on the Gemini North telescope provided additional vertical emissivity profiles for H_3^+ in Jupiter's auroral regions (Kedziora-Chudczer et al., 2017). The study analyzed the 2 μm overtone band emissions and determined that the peak column density of H_3^+ in the northern and southern auroras was approximately 4.5×10^{16} m^{-2}, with rotational temperatures around 950 K. Vertical profile ion densities were similar to prior measurements (Lam et al., 1997; Uno et al., 2014) and included estimates for the main Io footprint auroral region, marking the first such measurement in that specific region. Observations during the Juno mission's first and fifth perijove using the Jovian Infrared Auroral Mapper (JIRAM) mapped the planet from 60°N to 60°S up to 700 km, with vertical distributions as function of latitude on the dayside (Migliorini et al., 2019). They characterized the H_3^+ volume mixing ratio, which was distributed symmetrically with latitude, as well as temperatures that increased with altitude. More recent Juno/JIRAM observations presented in Migliorini et al. (2023) reveal significant variability in the exospheric temperature with time, following elevated H_3^+ temperature profiles at ~550 km, attributed to vertically propagating waves. In situ measurements by Juno/JADE provided direct observations of ion species in Jupiter's high-latitude ionosphere, showing that H^+ dominates the topside region above 4,000 km, with densities up to ten per cubic centimeter (Valek et al., 2019). These data offer valuable benchmarks for comparing remote sensing measurements of H_3^+ with local plasma conditions.

Most studies that derive temperatures and densities from H_3^+ spectra of the giant planets assume that the ion emits in a state of local thermal equilibrium (LTE). However, in regions of high temperature and low density (i.e., at high altitude) this assumption may break down. Models have attempted to account for the departure of H_3^+ populations from LTE (Melin et al., 2005), which reduces the intensity of IR emissions at high altitudes, tending to zero beyond 1,500 km above the 1 bar level.

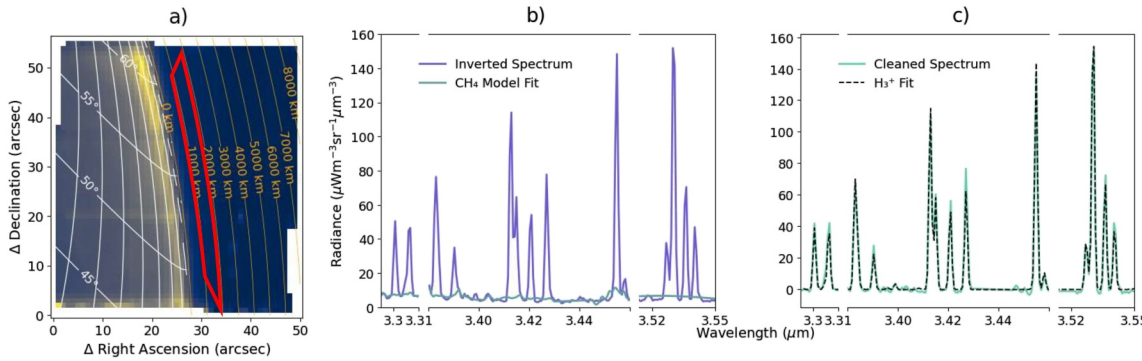

Figure 1. Observational set up and spectrum example at 55°N between 3.29 and 3.55 μm using the method from Melin et al. (2024). (a): IFU spectral image with overlaying latitudes and longitudes (white) and altitudes above the 1-bar pressure level (orange). The red rectangle indicates the altitude range from which the spectrum example for panels (b) and (c) is being extracted. (b): Processed NIRSpec spectrum after applying Tikhonov inversion (purple) with overlaying fundamental and hotband CH_4 lines and background fits (blue); (c): Extracted spectrum after cleaning (cyan) and corresponding *h3ppy* fitted spectrum (dashed).

Simultaneously examining both H_3^+ and electron density (N_e) profiles allows us to resolve the structure of individual ionospheric layers and determine the extent to which these layers adhere to model expectations, such as those under photo-chemical equilibrium (PCE). As noted by Mendillo et al. (2022), discrepancies between Ne and ion profiles—especially in dawn-dusk asymmetries—highlight the importance of transport processes and non-equilibrium dynamics that cannot be captured by analyses focusing on a single species alone. With Juno's radio occultation experiments (ROX), which began in 2023, the opportunity arose to plan simultaneous observations of H_3^+ profiles and N_e profiles. Hence, JWST programme #3665 was planned to coincide with Juno's ROX during perijove 54.

The aim of this study is to present the pole-to-pole, dusk and dawn, vertical H_3^+ temperature and density profiles observed during this programme. In Section 2, we present an overview of the programme and introduce the spectral cleaning and fitting procedures. Results are presented in Section 3, followed by a discussion in Section 4. Our conclusions are given in Section 5.

2. Observations and Data Reduction

JWST programme #3665 focused on scanning the entirety of Jupiter's limb in a clockwise direction, starting from Juno's ROX location on the dawn limb around 35°N at 10:45 UT on 2023-09-07, then moving clockwise around the planet. The programme captured 36 individual observations, each containing 4 dithers, half on the dawn side and half at dusk, every 10° latitude, for a total of 22.18 hr of observation time. Due to loss of guide star, 5 observations at dusk were lost: 65°N and 55°N were recovered on 2023-12-21 at 320°W and 292°W respectively, 45°N was observed on 2024-01-14 at 135°W, 35°N and 25°N were recovered on 2024-01-31 at 205°W and 220°W respectively. A list of each observation with its corresponding planetocentric latitude coverage (±10°), median longitude, UT of the observation and local-time at limb is provided in Appendix A. In addition, a complete view of all data points from the four dithers projected onto the planetary disk is included in Figure S1 in Supporting Information S1.

We used the NIRSpec (Jakobsen et al., 2022) Integral Field Unit (IFU) F290LP/G395H filter/grating, which covers spectral regions between 2.87 and 5.14 μm. This allows us to capture strong H_3^+ emission lines between 3.2 and 3.5 μm where absorption of sunlight from deep CH_4 makes this region spectrally dark. We use a 4-point nod to provide complete coverage of 5 × 5 arcsec per each individual observation, resulting in ∼319 km/spaxel resolution. By combining 4 groups in 1 integration, a S/N of ∼10 is achieved at an altitude of 1,000 km above the 1-bar level. An example spectral image and spectrum are shown in Figure 1. Figure 1a shows dither-combined IFU frame, integrating the spectrum between 3.29 and 3.55 μm, with the altitude range, longitudes, and latitudes indicated as contours. Whilst deep CH_4 absorbs sunlight, there is also a high altitude non-LTE solar pumped CH_4 emissions present at around 3.3 μm (Melin et al., 2024). Hence, we subtract modeled fundamental and hotband CH_4 emissions, as well as a polynomial background (Figure 1b), as in Melin et al. (2024). The isolated H_3^+ spectrum is shown in Figure 1c, along with a H_3^+ spectral fit. This procedure is performed at each latitude-altitude bin; as described below.

The NIRSpec IFU spectra of the individual dithers are binned onto a latitude-altitude grid with a resolution of 7° latitude × 225 km altitude up to 5,000 km, and then a median line-of-sight (LOS) spectrum is generated for each bin. There is a median of ∼62 spectra per bin across all bins. This approach ensures that the resulting spectra better represent the underlying emissions by reducing noise while still capturing vertical trends in the data. Whilst we detect H_3^+ emissions up to 9,000 km, this study presents results for up to 5,000 km altitude to reduce uncertainties and to focus on rendering fine details in the data set at multiple different latitudes and altitudes, while still maintaining a good signal-to-noise (S/N). Because of the complexity of the on-disk Jupiter spectrum at the very high sensitivity that JWST offers, we limit the vertical profiles to altitudes >750 km. This has the unfortunate side-effect of (likely) missing the main H_3^+ peak at around ∼350 km (Grodent et al., 2001), which introduces a bias when comparing total column densities with previous ground-based or modeled estimates that include the full vertical extent. Despite this limitation, these observations provide a unique view of Jupiter's ionosphere and enable the first pole-to-pole characterization of its vertical structure.

In the presence of a bright object, the JWST optical system produces a bright diffraction spike that can contribute significant radiance to adjacent pixels (Perrin et al., 2014). The disk of Jupiter contains very bright emissions, with intricate morphological structures, and each of these features has a diffraction pattern associated with it. As a result, we expect some of the observed signal above the limb to be a result of diffraction from features on the planet, which requires a correction. Whilst the correction required is inherently complex, we assume a first order single correction factor that is a function of distance from the planet, and is constant in latitude. To characterize this, we measure the median emission between 2.9 and 3.1 μm present above the 1 bar limb, a region dominated by solar reflectance from hydrocarbons (Sromovsky & Fry, 2010). We assume that these emissions are within the radiance uncertainty at 5,000 km, which allows us to produce a correction factor as a function of altitude that is applied to all the vertical LOS profiles.

In order to convert the binned, cleaned, and diffraction corrected LOS H_3^+ spectra observed above the limb (units of $Wm^{-2}sr^{-1}\mu m^{-1}$) to obtain local ionospheric properties, we apply a vertical inversion to produce spectra of volumetric emission (units of $Wm^{-3}sr^{-1}\mu m^{-1}$). These spectra are then fitted using the open source Python package *h3ppy* (Melin, 2025), for example, see Figure 1c, to retrieve the local ion density and temperature. For the inversion we apply the Tikhonov regularization technique (Tikhonov & Arsenin, 1977) which allows us to control error growth and smoothing factors. This inversion method has been used on Mars occultation analysis (Gröller et al., 2018; Quémerais et al., 2006) as well as Cassini data (Koskinen et al., 2011). Additionally, Tikhonov regularization has been applied in JWST/NIRSpec Fixed Slit spectral extractions, where it has been used to optimize signal recovery and mitigate noise in planetary and trans-Neptunian object observations (Denneulin et al., 2023). For profiles above 60° latitude, we use a smoothing factor $\lambda = 0.03$. For mid-latitudes and low latitudes we use $\lambda = 0.13$ to balance the S/N and vertical smoothing of the profiles introduced by the Tikhonov inversion. Our choice of smoothing factor aimed to stabilize the inversion as minimally as possible while still applying a necessary correction to suppress noise and prevent overfitting to small-scale variations. This ensures that the retrieved profiles remain as faithful as possible to the observed data while maintaining a physically reasonable vertical structure. To quantify the uncertainties introduced by the inversion process, we generated 1,000 synthetic local volumetric density profiles, forward-modeled them into LOS-integrated profiles, and then re-inverted each using the same Tikhonov algorithm applied to the JWST data. This process allowed us to assess how well the inversion recovers known input profiles under realistic noise conditions. The resulting errors were averaged across iterations at each altitude to compute the mean and standard deviation, shown in Figure S2 in Supporting Information S1. The analysis demonstrates that retrieved values are generally well constrained below ∼3,000 km, with typical inversion errors under 10%, but become increasingly uncertain at higher altitudes. Above 3,000 km, the uncertainty grows rapidly, often exceeding 40%–60%, indicating that the inverted profiles are poorly constrained in this region. This highlights the limits of spectral inversion at high altitudes and should be considered when interpreting vertical trends beyond this range.

The *h3ppy* spectral retrievals of each binned, cleaned, diffraction corrected, and inverted H_3^+ spectrum yields the temperature and ion density, as well as the total H_3^+ emission (i.e., the radiative cooling rate), along with their associated uncertainties. The S/N of the data largely governs the magnitude of the uncertainties, and the largest errors are found where the signal is the weakest (e.g., equatorial latitudes at dusk).

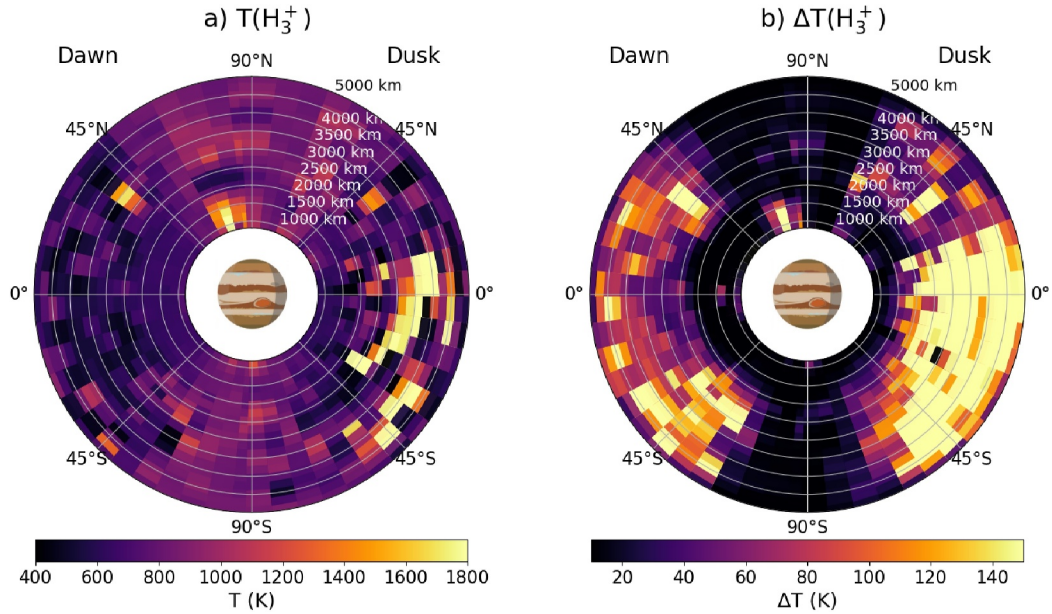

Figure 2. H_3^+ global vertical temperature map (a) and respective errors from the fitting routine (b). Each data point is binned as 7° latitude × 225 km altitude up to 5,000 km. Temperatures appear relatively constant in altitude, with temperature-latitudes gradients from poles to equator (see Figures 5a and 5b). We note localized heating at both poles in the auroral region, particularly in the north pole (see Figure 4 for these vertical profiles).

3. Results

By performing the spectral inversion and fitting routine illustrated in Figure 1 on all profiles available from pole-to-pole at dawn and dusk, we derive a global vertical temperature map (Figure 2a), T(H_3^+). We note that at lower latitudes, particularly at dusk, errors are larger (Figure 2b). This is due to fainter H_3^+ emissions at the equator and sub-auroral regions, producing a smaller S/N. As mentioned in Section 2, results above 3,000 km are poorly constrained from the inversion technique but are reported here for future modeling purposes. Nonetheless, these JWST profiles are the highest fidelity vertical profiles of the low latitude ionosphere ever captured. We report median values in Table 1 to better represent the central tendency in data sets with potential outliers and non-Gaussian distributions. Mean values were also computed and found to be consistent with the medians within uncertainties. The northern aurora (≥55°N) has median temperatures for altitudes up to 2,000 km of 876.8 ± 15.25 K and 874.5 ± 17.30 K at dawn and dusk respectively, the southern aurora (≥55°S) has median temperatures of 838.5 ± 10.70 K and 803.0 ± 13.45 K at dawn and dusk, respectively, and the rest of the planet shows approximately vertical constant temperatures with medians of 654.5 ± 9.00 K and 652.5 ± 20.75 K at dawn and dusk. The apparent hemispheric asymmetry in auroral temperatures is primarily due to greater spatial coverage of

Table 1
Summary of Median Temperatures and Densities in Different Regions (From Figures 2a and 3a) and Respective Median Errors (From Figures 2b and 3b) for All Altitudes Up to 2,000 km

	Dawn				Dusk			
	(K)		(m^{-3})		(K)		(m^{-3})	
Region	T	**ΔT**	**n**	**Δn**	T	**ΔT**	**n**	**Δn**
North Aurora	876.8	15.25	1.42×10^8	0.07×10^8	874.5	17.30	6.08×10^8	0.29×10^8
Non-Auroral	654.5	9.00	1.10×10^8	0.07×10^8	652.5	20.75	5.04×10^7	1.20×10^7
South Aurora	838.5	10.70	1.53×10^8	0.06×10^8	803.0	13.45	9.60×10^7	0.61×10^7

Note. The non-auroral region is defined as <55°N and <55°S, while the north and south auroral regions are defined as >55° North and South respectively.

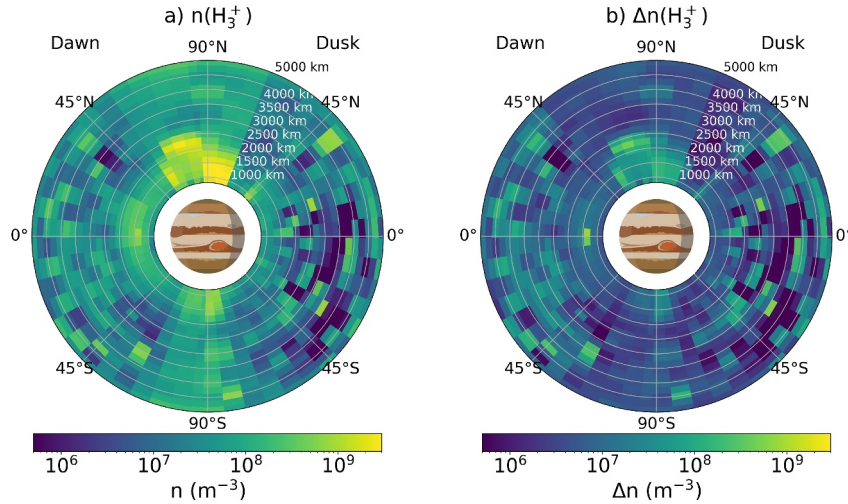

Figure 3. Global vertical map for H_3^+ number density (a) and its respective errors (b). As opposed to Figure 2, vertical profiles here present much more variability, decreasing by two orders of magnitude in altitude. Particularly, we highlight the stark dawn-dusk asymmetry, with dawn exhibiting more than twice the density of dusk at low latitudes. The enhancement between 40°N–50°N is further explored in Figure 7.

the northern auroral region in the JWST data set (see Figure S3 in Supporting Information S1), whereas the southern aurora was only partially sampled, capturing just a limited glimpse of the emission.

Figure 3 shows the first observed vertical volumetric H_3^+ density profiles, n(H_3^+), across all latitudes. In general, the dawn limb shows higher densities up to 2,000 km than dusk, with medians (excluding auroral regions) of $1.10 \pm 0.07 \times 10^8$ at dawn and $5.04 \pm 1.20 \times 10^7$ at dusk. Beyond the expected auroral enhancements, we observe a notable sub-auroral density enhancement at dusk between 50 and 40°N. This feature corresponds to observations acquired at later dates and different SIII longitudes (see Figure 7), suggesting that temporal and longitudinal variability may be contributing factors. The combination of observations from multiple dates in this latitude band likely introduces variability in thermospheric structure. Overall, n(H_3^+) profiles seem to present much more variability across latitudes and altitudes compared to T(H_3^+) in Figure 2a. As before, we also present corresponding profiles errors in Figure 3b.

Figure 4 shows the northern polar temperature and density profiles, where auroral emissions were captured at the time of observations. This is reflected by the localized heating up to 1,500 km of altitude from latitudes 68°N to 88°N at dawn (Figure 4a). Profiles are here reported up to 3,000 km as above this altitude the LOS inversion technique poorly constrains spectra (see Figure S2 in Supporting Information S1). The profile at 74°N in particular reaches temperatures up to ∼1900 K at 1,000 km. These high temperatures then quickly decrease to ∼600 K between 2000 and 2,500 km for all latitudinal profiles excluding 60°N, which remains constant in altitude. While the profiles are constructed by binning all available observations by latitude—without preserving individual SIII longitudes—the observed heating at 74°N falls within the known auroral latitudinal region. A full overview of the observation geometry, including all contributing SIII longitudes from all dithers, is shown in Figure S3 in Supporting Information S1 for reference. At dusk (Figure 4b), temperatures do not present the same stark peak as Figure 4a but profiles at 60°N, 68°N and 88°N show temperature peaks of 1100 K at 3,250 km, 2,250 km, and 3,000 km, respectively. On the other hand, temperature profiles at 74°N and 82°N remain largely constant in altitude. Dawn auroral density profiles (Figure 4c) show a localized density peak at ∼2,000 km with a maximum of 3×10^9 m^{-3}, which drops to a minimum of 2×10^7 m^{-3} between 2,500 and 3,000 km. As in Figure 4a, the profile at 60°N is unaffected by the density enhancement happening at higher latitudes, and rather shows a profile peaking at 1,000–1,250 km, closely matching the shape of profiles at 74°N, 82°N and 88°N on the dusk side (Figure 4d). In the dusk side, densities seem to separate in two distinct populations: the three northern-most profiles reach a maximum 4×10^9 m^{-3} at lower altitudes (1,000 km), then drop by one order of magnitude in density; the second group of profiles show two different peaks in altitude per profile, 60°N peaks at ∼2000 km and 3,500 km, and 68°N

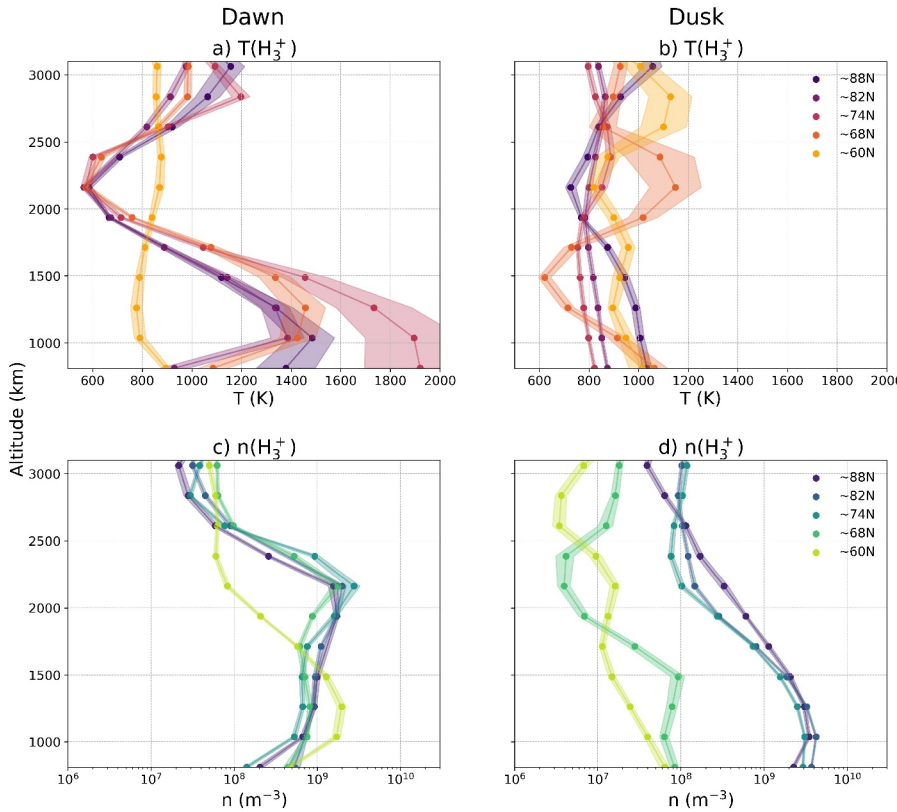

Figure 4. North pole H_3^+ temperature vertical profiles at ~60°N, ~68°N, ~74°N, ~82°N, ~88°N. (a): Dawn profiles; (b): Dusk profiles. Temperatures reach up to 1900 K at dawn during the aurora event captured in the observations. However this heating appears to be confined at low altitudes, rapidly decreasing then remaining constant higher up in the ionosphere.

peaks at 1,500 km and between 2,500 and 3,750 km, with lower density values ranging from 4×10^6 m^{-3} to 1×10^8 m^{-3}.

We explore more closely T(H_3^+) and n(H_3^+) variations across all latitudes for altitudes centered on 1,040, 1,490, 1,710, and 1,940 km in Figure 5. Figures 5a and 5b exemplify the trend seen in Figure 2a: temperatures seem to generally be constant in altitude, except for localized auroral heating at ~1,040 and 1,490 km seen in the north pole. Away from the poles, dusk presents more altitudinal variability than dawn, however, as per Figures 2a and 2b, uncertainties are larger above 1,500 km due to the smaller S/N. As in Figure 3a, n(H_3^+) presents more global variability in altitude (Figures 5c and 5d). In particular, at dawn densities reach 10^9 m^{-3} in the northern pole and 3×10^8 m^{-3} in the southern. Densities then quickly decrease to 10^7 m^{-3}–10^8 m^{-3} away from the poles. While the drop in density equator-ward happens at ~1,000–1,250 km for altitudes above ~1,940 km, in the middle of the ionosphere (~1,490–1,700 km) there is an enhancement of almost one order of magnitude away from the sub-auroral regions, below ~60° north and south. At dusk, Figure 5d, a similar trend is seen, with n(H_3^+) dropping by two orders of magnitudes with altitude. Here, values are generally lower than dawn: 10^7–10^8 m^{-3} away from the equator. Both poles, however, show density increases in altitude up to 1,700 km and then decreases, as also shown in Figure 4d. We also calculate column integrated values: T(H_3^+) present median values of 684.4 ± 12.5 K and 676.6 ± 13.0 K planet-wide at dawn and dusk, respectively; median column integrated densities, N(H_3^+), are $4.02 \times 10^{14} \pm 4.73 \times 10^{13}$ m^{-2} at dawn and $2.36 \times 10^{14} \pm 4.02 \times 10^{13}$ m^{-2} at dusk planet-wide, with maxima of $2.26 \times 10^{15} \pm 2.02 \times 10^{14}$ m^{-2} and $4.12 \times 10^{15} \pm 4.83 \times 10^{14}$ m^{-2} at dawn and dusk in the northern hemisphere. It is important to note that these values only include contributions from altitudes above 750 km due to observational constraints, and therefore they might underestimate the true total column densities—particularly as they omit the expected peak in H_3^+ density near 350 km. Both temperatures and densities appear more variable at dusk across latitudes than at dawn, noting that dusk generally presents higher errors (Figures 2b and 3b).

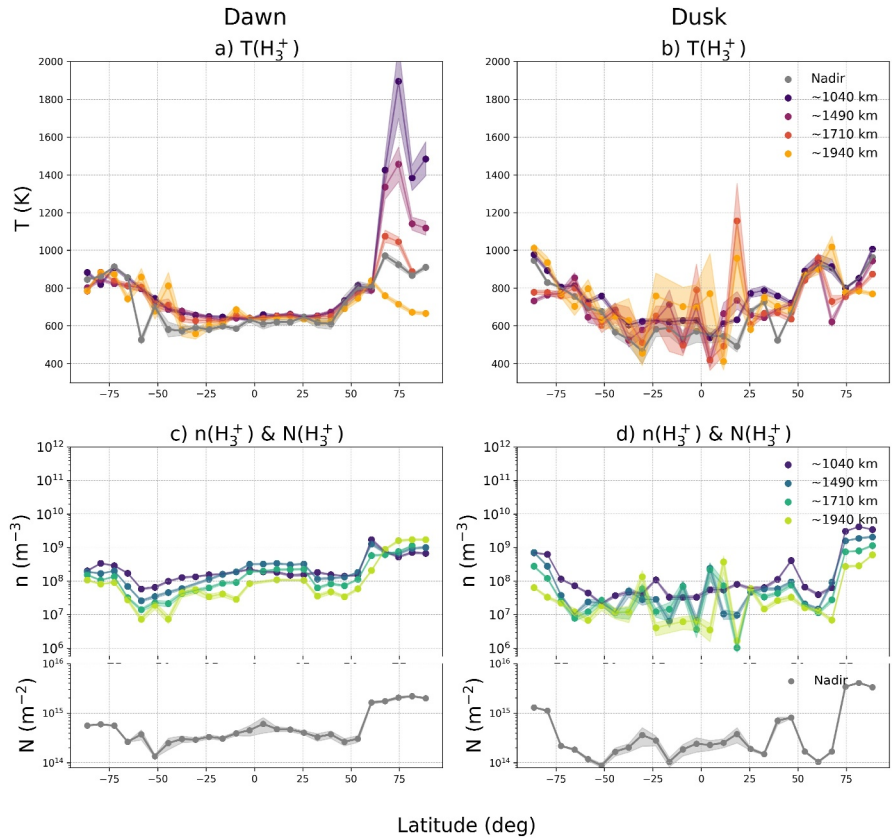

Figure 5. Dawn and dusk (left and right columns) H_3^+ temperatures and densities (top and bottom) across all latitudes at ~1,040 km, ~1,490 km, ~1,710 km, ~1,940 km as well as correspondent column integrated ("nadir"). Panels (a) and (b) highlight how temperatures remain generally constant in altitude, as observed in Figure 2, while densities (panels c and d) decrease with altitude (see Figure 3).

Using the fitted temperatures and densities, we calculate the volumetric total emission as per Miller et al. (2013), E(H_3^+). Figure 6a shows the radiative cooling effect that E(H_3^+) has on the local vertical atmosphere. Features seen in Figures 2a and 3a of local enhancements at lower altitudes in the polar and auroral regions are reflected here, reaching high E(H_3^+) values of 10^{-10} $Wm^{-3}sr^{-1}$. E(H_3^+) at the poles is radiated to space, highlighting the localized

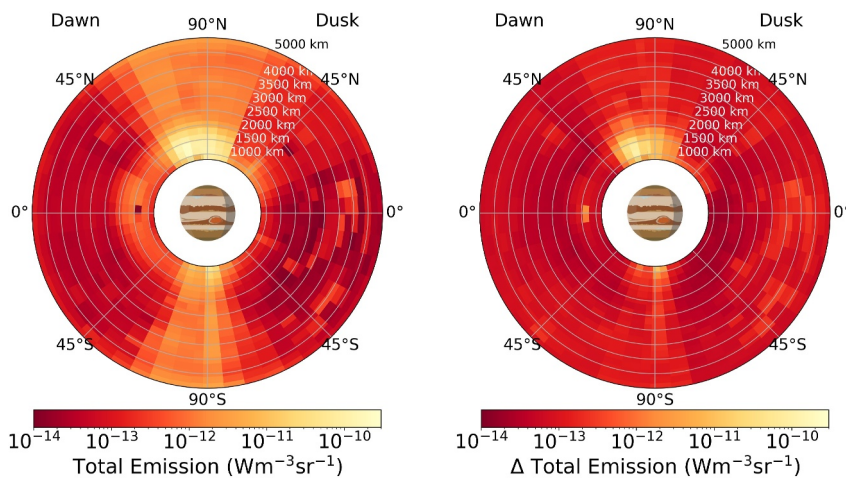

Figure 6. Total emission calculated from T(H_3^+) and n(H_3^+) as per Miller et al. (2013) (panel a), with respective errors (panel b). The total emission indicates how much energy is radiated to space.

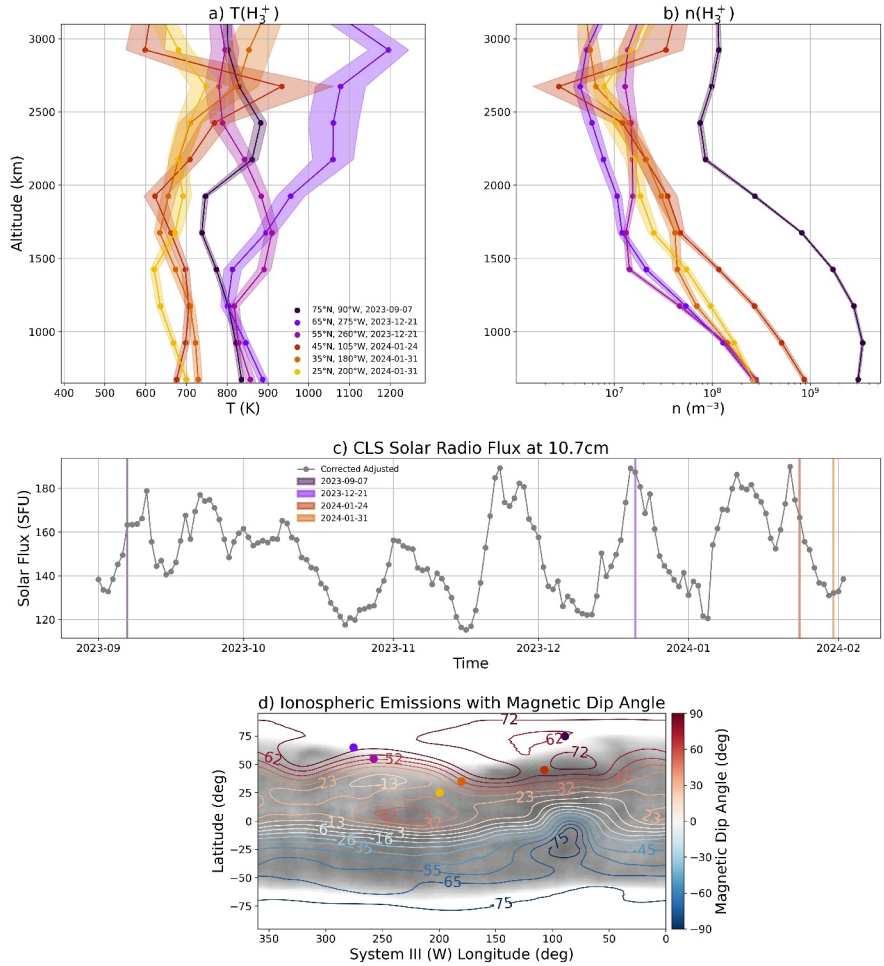

Figure 7. Dusk northern vertical profiles at ∼65°N, ∼75°N (observed on 2023-12-21), ∼45°N (on 2024-01-24) and ∼25°N, ∼35°N (on 2023-01-31) compared to the rest of the data set observed on 2023-09-07 (here ∼75°N). These profiles are binned by 10° latitude to maintain a good S/N for each date and is not binned with nearby values. (a and b): Temperature and density profiles, respectively, showing latitudinal variation and altitudinal variation with several peaks. (c): Time series of the Collected Localization Satellites (CLS) solar radio flux measured at Earth at 10.7 cm adjusted to 1 AU with interpolated data gaps and flare correction, indicating the solar activity during the observation periods. We retrieved F10.7 cm values from Nobeyama Radio Polarimeters, with additional processing from Space Weather Services at CLS. (d): Global map of ionospheric H_3^+ emissions from Stallard et al. (2018) overlaid with magnetic dip angle contours, illustrating how different regions of the ionosphere align with the planetary magnetic field. Colored scatter points mark the locations of the density and temperature measurements shown in panel (a) and (b).

cooling effect noted also in Figure 4. Similarly to Figures 3a and 5c, dawn presents an enhancement in E(H_3^+) between 1,500 and 2,000 km too, which, as in the case of T(H_3^+) and n(H_3^+), does not significantly affect altitudes above that region. Another feature to note is the E(H_3^+) enhancement at dusk adjacent to the northern sub-auroral region. This coincides with a corresponding n(H_3^+) enhancement seen in Figure 3a. These profiles originate from observations acquired 3–4 months after the main observation set, and therefore reflect different SIII longitudes and potentially different magnetospheric conditions. While the spatial location of this feature aligns with known sub-auroral latitudes, we acknowledge that temporal variability—such as changes in thermospheric dynamics or magnetospheric input—as well as longitudinal differences in Jupiter's auroral morphology, may have influenced the observed enhancement. As such, this feature likely reflects a combination of local plasma processes and the time-varying nature of the observation geometry, and should be interpreted in that context. Additionally, using pole-to-pole retrieved E(H_3^+) measurements, we calculate the expected global radiative cooling by H_3^+ to be $4.10 \times 10^{13} \pm 5.30 \times 10^{11}$ Wsr^{-1}. While this estimate assumes the observed limb profiles are representative of the ionosphere as a whole, it is important to note that the exclusion of altitudes below 750 km introduces a bias, as

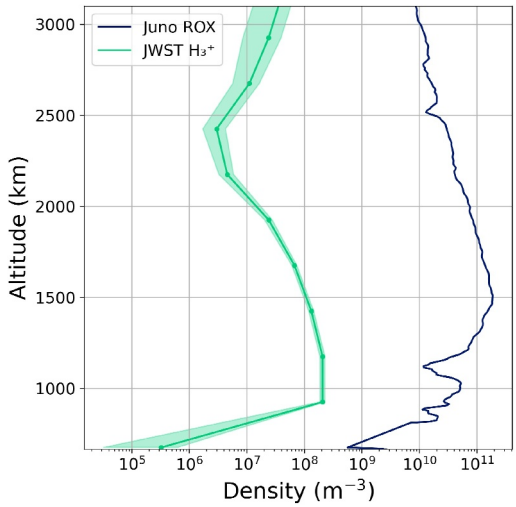

Figure 8. Comparison between the volumetric H_3^+ density profile retrieved from JWST observations at 35°N dawn at ∼151°W (10° latitude bin) and the electron density profile from Coffin et al. (2025) obtained from Juno Radio Occultation (ROX) during Perijove 54 ingress (PJ54N) at 168°W.

it omits the region where H_3^+ emissions are expected to peak. Furthermore, these measurements are limited to the terminator region, where H_3^+ densities are likely lower than those expected near local noon.

We investigate T(H_3^+) and n(H_3^+) profiles from the recovered observations, separating them by date, in Figures 7a and 7b to investigate the temporal evolution of the ionosphere. As in Figure 4, we report profiles up to 3,000 km. Unlike all previous results where data are binned in 7° latitude increments to improve S/N by combining multiple observations, here we use individual IFU data sets for each observation date, resulting in a coarser 10° latitude binning. This approach preserves temporal and spatial variations in the ionosphere, allowing direct comparisons between profiles taken on different days. We compare a high latitude profile at 75°N taken during the first JWST visit as a reference for, and comparison to, the recovered observations. Profiles at 65°N and 55°N, taken on 2023-12-21, display high-altitude temperature peaks, which align with the multi-peak structures in Figure 4b and the second population of density profiles in Figure 4d. Meanwhile, the 45°N profile shows density enhancements at 3,000 km and 4,000 km, despite similar solar conditions on 2024-01-24 and 2023-09-07. The lower solar flux on 2024-01-31 (by 30 SFU) does not appear to significantly impact the 35°N and 25°N profiles, which remain comparable to those at 45°N and 55°N, with a temperature peak at 3,000 km also present at 35°N. Figure 7d maps the profiles to the magnetic dip angle, which is the angle between the magnetic field line and the local horizontal surface, with the underlying H_3^+ ionospheric emission map from Stallard et al. (2018). We use JRM33 and Con2020 (Connerney et al., 2020) as internal and external field models respectively, with the JupiterMag community code (Wilson et al., 2023). We note that the profile at 45°N in Figure 7b, is located near a localized high magnetic dip angle region (∼ 72°), as opposed to profiles at 55°N and 65°N which were observed between 260 and 275°W, with lower magnetic dip angle (∼52°–62°). In particular, we highlight that this profile was observed at a different System III longitude (∼80–120°W), compared to 55°N and 65°N (∼260–275°W). Kurth et al. (2025) showed that electron densities in Jupiter's ionosphere vary significantly with SIII longitude, with pronounced minima near the "Great Blue Spot" (∼75°W) and enhancements between 150°–250°W. Thus, the variability observed at 45°N may be partially attributed to longitudinal structure in the ionosphere, influenced by Jupiter's complex magnetic morphology. While in the rest of our study we focus on binning by latitude to boost signal-to-noise and do not track individual SIII longitudes, we note that profiles from different dates inherently sample different SIII sectors, which can modulate plasma properties via localized field-aligned transport and particle precipitation.

Figure 8 compares the JWST-derived volumetric H_3^+ density profile at dawn near 35°N at ∼151°W (green line, from a 10° latitude bin) with the electron density profile retrieved from the Juno PJ54 ingress radio occultation experiment (blue line) (Coffin et al., 2025) at a similar latitude at 168°W. The JWST profile peaks at 1–2 × 10^8 m^{-3} just below 1,000 km altitude, while the Juno ROX profile shows electron densities exceeding 10^{11} m^{-3} at 1,500 km. The JWST limb profile begins at 750 km, and thus does not capture the low-altitude peak observed in the Juno profile. Above 1,000 km, both profiles decrease with altitude, but the ROX profile declines more rapidly. This comparison highlights the consistency in vertical trends while also illustrating the much higher total electron density of three orders of magnitude compared to the retrieved H_3^+ contribution. Further, the JWST and Juno profiles were obtained at similar latitudes, but with different longitudes— ∼20° longitude difference— introducing a potential influence of magnetic field variations on the observed differences in peak altitude and shape.

4. Discussion

In contrast to previous Juno/JIRAM observations of the dayside equatorial vertical profiles (Migliorini et al., 2019, 2023), in Figure 2a we do not observe much altitudinal variability in temperature at sub-auroral and equatorial latitudes. Rather, it appears that temperatures remain relatively constant in altitude at ∼600 K (Figures 5a and 5b), whereas JIRAM observed heating of 860–1000 K in sub-auroral regions between 48°N and 55°N at altitudes of 700–1,000 km (Dinelli et al., 2019). However, it is of note that the maximum altitude obtained from

JIRAM vertical profiles is 1,000 km and results presented here start around ∼750 km. In addition, differences in how the data were collected and analyzed may also explain the discrepancy. JIRAM used limb observations from several different flybys taken over a 2-year period Migliorini et al. (2019), while the majority of our JWST data were obtained within a single 24-hr window. Unlike JIRAM, which was able to observe altitudes below 750 km, we do not capture temperature structures below this altitude in our data set. Together, these differences in altitude coverage, observation timing, and analysis methods likely all contribute to the differing temperature structures observed.

In the northern vertical profiles presented here (Figure 4a) the temperatures at ∼68°N are approximately 200 K hotter than the ones observed with Juno/JIRAM between 700 and 1,000 km (Dinelli et al., 2019). With NIRSpec IFU's sensitivity, we are able to observe that this heating is localized strictly to limited latitudes and in this occasion did not significantly affect lower latitudes (e.g., ∼53°N). In addition, this temperature quickly decreases to 600 K at 2,000 km, followed by a secondary peak for polar latitudes at ∼3,000 km, and becomes constant with increasing altitude, with values between 820 and 900 K. While individual SIII longitudes are not resolved in our latitudinal binning, the ∼68°N profile lies within the typical auroral latitude range. Figure S3 in Supporting Information S1 provides an overview of our limb observation geometry across all longitudes, offering context for how this profile relates to known auroral boundaries, although no direct comparison with Juno/JIRAM emission maps is made. A qualitatively similar profile structure was produced by Yates et al. (2020) with a 3D magnetosphere-ionosphere-thermosphere (MIT) model. Although vertical shapes are similar, the profiles with larger temperature peaks observed are at ∼68°N and ∼74°N, rather than at ∼81–88°N, as predicted by their model, although longitudes are not directly comparable. In addition, all four profiles peak at 700–1,000 km in Figure 2a and are hotter compared to the auroral peak presented in Yates et al. (2020) of ∼820 K at 500 km. It is worth nothing that perhaps these differences derive from the model's limitations such as fixed Pedersen conductances between ±60–75° latitude and an asymmetric magnetosphere model, as well as the expected inherent variability in the auroral region. Finally, their model is limited to ∼1,400 km, and it is therefore difficult to compare and explain the secondary peak we observe at ∼3,000 km. However, the lower altitudinal peak can be attributed to ionospheric Joule heating in the auroral region as modeled in Bougher et al. (2005).

Auroral H_3^+ density profiles from Figure 4c are one to two orders of magnitude lower than results from Tao et al. (2011), although noting that their emission intensity is considered to be in steady state conditions in the model and that the relationship between auroral electrons, atmospheric heating and H_2 vibrational states are not incorporated. In Figure 3a, non-auroral dawn densities present values up to 3×10^8 m^{-3} up to 1,700 km (also seen in Figure 5a). These values exhibit higher-altitude peaks than those observed at dusk, where densities of ∼8–9 $\times$ 10^7 m^{-3} peak at 700 km. This comes somewhat as a surprise considering that if the ionosphere at Jupiter were to follow photochemical equilibrium (PCE) theory, the opposite should be observed, see Mendillo et al. (2022). PCE occurs when ion production, chemical reactions, and recombination processes reach a balance at a given location, leading to an ionospheric density primarily controlled by local photochemistry rather than transport or other external drivers. Since ion production at Jupiter is dominated by H_2^+ (∼ 90%) with a smaller fraction of H^+ (∼10%) and since the reaction $H_2^+ + H_2$ is rapid, nearly all H_2^+ production leads directly to H_3^+. While H^+ production is relatively slow, its long lifetime allows it to become the dominant ion, which, combined with its small diurnal variation, results in relatively little change in the total electron density (N_e). On the other hand, H_3^+ is rapidly created and rapidly destroyed, leading to a first-order symmetric diurnal variation with a peak near noon. However, this symmetry is slightly broken due to Jupiter's rapid rotation and the reaction $H^+ + H_2 \rightarrow H_2^+ + H$, which enhances H_2^+ production. This effect can shift the H_3^+ peak slightly past noon and should result in higher densities at dusk than at dawn—see Moore et al. (2019). At Earth, the ionosphere exhibits higher plasma densities at dusk compared to dawn. This is because at dusk, solar radiation has only just ceased, maintaining higher ionization levels, whereas at dawn, an entire night of chemical recombination has reduced the plasma density before solar radiation resumes, leading to the minimum density just before sunrise (Walsh et al., 2014). Similarly, at Saturn, enhanced electron densities are observed at dusk, compared to dawn (Moore et al., 2006). At Jupiter, dawn-dusk H_3^+ densities were predicted by modeling to behave similarly to the Earth and Saturn (Achilleos et al., 1998). However, the reanalysis of Galileo's ROX in Mendillo et al. (2022) showed that electron profiles at dawn have larger maximum electron densities than values at dusk, similar to what is observed here. Additionally, in situ observations by Juno/JADE show that the auroral topside ionosphere contains cold H^+ ions with densities on the order of tens of cm^{-3} above 4,000 km (Valek et al., 2019), providing a useful high-altitude

comparison to the limb-derived H_3^+ densities presented here. At these high altitudes, however, the density of H_2 becomes sufficiently low that the efficient production of H_3^+ via the $H_2^+ + H_2$ pathway is expected to diminish significantly, which likely contributes to the increasing uncertainty and potential underestimation of H_3^+ densities retrieved above 3,000 km in our profiles.

The comparison between JWST and Juno ROX profiles emphasizes the value of combining complementary data sets to characterize Jupiter's ionosphere. H_3^+ densities retrieved from JWST are several orders of magnitude lower than the total electron densities measured by Juno ROX at comparable altitudes, reaffirming that H_3^+ remains a minor ion species in Jupiter's mid-latitude ionosphere. This aligns with expectations from ionospheric models (Moore et al., 2019), where long-lived H^+ dominates the electron population, while H_3^+ is rapidly produced and destroyed, leading to more pronounced diurnal variability. Moreover, the JWST limb geometry provides sensitivity to higher altitudes with lower vertical resolution, while Juno's radio occultation yields fine-scale structure at lower altitudes. As shown by Kurth et al. (2025), in situ electron densities derived from the Juno Waves instrument exhibit strong organization with respect to System III longitude. Since the JWST and PJ54 profiles were acquired at different longitudes ($\sim$151°W vs. $\sim$168°W), these spatial variations may influence the vertical ionospheric structure, possibly via magnetic topology or longitudinally modulated neutral winds. These effects underline the importance of considering longitude when interpreting ionospheric profiles from different data sets.

The observed H_3^+ density asymmetry between dawn and dusk, particularly at non-auroral latitudes, appears to mirror some of the large-scale variability reported in electron densities by Juno/Waves. Specifically, Kurth et al. (2025) report significant orbit-to-orbit differences in topside electron density profiles, with pre-dawn densities occasionally exceeding dusk values by up to an order of magnitude. Kurth et al. (2025) emphasize that this variability is well-organized by longitude and likely influenced by magnetic topology. Results also highlight substantial variability in ionospheric density on both short and long timescales, with densities ranging from a few hundred cm^{-3} to 80,000 cm^{-3} at altitudes above 3,500 km, where thermal effects and scale height differences may also contribute. Rather than indicating a fundamentally non-photochemical origin for the observed H_3^+ densities, these results underline that large-scale structure and asymmetries—like those seen in the JWST dataset—may reflect longitudinal and magnetospheric influences.

Both Figures 5a and 5b seem to broadly agree with previous measurements of $T(H_3^+)$ across the disk observed with Keck II/NIRSPEC (O'Donoghue et al., 2021). As we are able to resolve vertical temperature profiles as a function of latitude, from Figure 5b we derive steeper dusk temperature gradients of $\sim$−4.4 K/degree between $\sim$1,000–1,500 km and $\sim$−2.2 K/degree latitude at all other altitudes, compared to Figure 5a which presents dawn temperature gradients of −2.4 K/degree (excluding auroral heating in the north up to 1,700 km). The dusk gradient at low altitude appears to be the closest to results presented in O'Donoghue et al. (2021). Gradients observed in their work are $\sim$−4.9 K/degree from 75°N to the equator and $\sim$−5.9 K/degree from 75°S to the equator. While gradients from O'Donoghue et al. (2021) are remarkably different to high altitude gradients observed in Figures 5a and 5b, sub-auroral and equatorial temperatures observed are in agreement ($\sim$600 K in Figure 5a and $\sim$550–600 K in Figure 5b). Overall, a comparison of temperature gradients at dawn and dusk at different altitudes taken closer in time to this data set would be more appropriate. This would be beneficial in the understanding of auroral region temperature variability and how it affects heat transport in the vertical upper atmosphere as a function of latitude.

The pole-to-pole profiles shown in Figures 5c and 5d, H_3^+ densities do not decrease exponentially with altitude, rather $n(H_3^+)$ profiles present several maxima and minima peaks vertically, for example comparing $\sim$1,040 and $\sim$1,940 km across all latitudes. This may be indicative of significant departures of the H_3^+ emissions from LTE. Non-LTE effects on H_3^+ emissions have been previously highlighted by Melin et al. (2006), who demonstrated that above $\sim$650 km, vibrational levels of H_3^+ become underpopulated due to the high rate of radiative de-excitation, affecting the observed emission intensity. Indeed, Tao et al. (2011) noted that IR emissions at Jupiter and Saturn are subject to significant non-LTE effects, especially at high altitude where the density is low and the temperature is high, which can lead to a scenario where the derived H_3^+ densities significantly underestimate the real value. Although a full non-LTE radiative transfer analysis is outside the scope of this work, we acknowledge that deviations from LTE could contribute to the observed vertical structure—particularly the rapid decrease in density above 2,000 km in auroral regions. Future studies combining H_3^+ and electron density

measurements (e.g., from Juno ROX) with detailed radiative modeling will be required to disentangle the relative contributions of non-LTE effects and atmospheric processes.

Density variation trends were seen in previous modeling (Barrow & Matcheva, 2011) as well as H_3^+ disk observations (Melin et al., 2024) and were attributed to effects of gravity waves on the ionosphere. Barrow and Matcheva (2011) concluded that n(H_3^+) is perturbed by chemical interactions with other perturbed ion species above 600 km, which could explain local perturbations in ionospheric layers. Gravity waves have also been directly inferred from temperature oscillations observed by the Galileo Probe during its descent into Jupiter's atmosphere (Matcheva et al., 2001; Young et al., 1997), providing strong in situ evidence for their presence and vertical propagation. As limb profiles taken by JWST covered a range of different longitudes, obtained at slightly different times, it is difficult with this data set to calculate wave phases across the planet, therefore it is challenging to fully compare it to the work in Barrow et al. (2012). Nonetheless, the significant variability in both the temperatures and H_3^+ densities presented here (at all latitudes), do seem to point at gravity waves driving density perturbations in the non-auroral ionosphere in light of the above mentioned models.

By integrating E(H_3^+) in Figure 6, we calculate the total radiative loss from dawn to dusk and derive 4.1 TW, which represents H_3^+ cooling power planet-wide. This is a stark difference to previous measurements by Lam et al. (1997) that derived 3.4 TW and 3.0 GW in the north and south pole with UKIRT, and from Juno/JIRAM measurements that reported 2,000–4000 GW (Gérard et al., 2023). Our NIRSpec/IFU observations are primarily sensitive to H_3^+ emission in the 3.2–3.5 μm range and cover only the sunlit limb, whereas earlier estimates from UKIRT and JIRAM included broader spectral ranges and global auroral regions, where H_3^+ densities and temperatures are elevated.

In general, an increase in the solar flux may be expected to produce increased H_3^+ densities, due to the increase in photoionization of H_2. However, vertical density profiles for the recovered observations show no clear relationship to the solar flux (Figure 7c). For example, the highest solar flux is seen for the observation on 2023-12-21, which shows the lowest densities (Figure 7b), and are very similar to the vertical density observed on 2024-01-31, which has the lowest solar flux. Stallard et al. (2018) mapped the H_3^+ radiance of the ionosphere at low latitudes, and showed that the strength of the emission is strongly linked with magnetic field topology, as recently reported also by Knowles et al. (2025). Assuming that this radiance is mostly driven by the density, then the local magnetic field environment that a particular vertical profile samples may strongly influence the observed densities. Figure 7d shows the radiance map of Stallard et al. (2018) with the magnetic dip angle as contours, and the latitude and longitude location of the vertical profiles in Figure 7b as circles. This shows a localized region of high magnetic dip angle ($\sim 72°$) around 55–100°W and 50°N, just above the dark ionospheric feature at 45–50°N. A high dip angle facilitates vertical plasma transport while restricting horizontal motion, which could explain the enhanced density profile at 45°N compared to other high-latitude profiles at different longitudes (Figure 7b). Although the dip angle at this location appears comparable to the two profiles around 275°W at 65°N and 75°N, suggesting additional local factors may be at play, that is, precipitation or magnetic field strength (Knowles et al., 2025). Overall, a number of processes are influencing global ionospheric H_3^+ distribution such as solar flux variability, magnetic field topology, plasma transport, gravity waves, and localized electrodynamic processes, some of which remain poorly characterized and require further investigation through combined observational and modeling efforts.

5. Conclusions

We have presented the first pole-to-pole dawn and dusk vertical temperature and density profiles from JWST programme #3665. The vertical H_3^+ temperature global map presented here shows generally constant temperature in altitude up to 2,000 km with medians of 876.8 and 874.5 K in the north pole, 838.5 and 803.0 K in the southern pole and 654.5 and 652.5 K for the rest of the planet, at dusk and dawn respectively. This is significantly different to previous Juno/JIRAM observations showing more vertical temperature variability (Dinelli et al., 2019; Migliorini et al., 2019, 2023). The JWST observations reported here were mostly obtained over the course of 24 hr, whereas Juno/JIRAM observations are the result of over 2 years of data. The northern auroral temperature profiles showed localized heating of up to ~1900 K at lower altitudes. This localized heating is highly confined in latitude and altitude. Further, it was possible to calculate temperature gradients for the first time with respect to

latitude at different altitudes across all latitudes. Steeper gradients were observed at dusk (∼−4.4 K/degree at ∼1,000–1,500 km and ∼−2.2 K/degree at all other altitudes) compared to dawn (∼−2.4 K/degree).

A vertical H_3^+ density global map showed densities of 10^8–10^7 m^{-3} up to 2,000 km. We observe a strong dawn-dusk asymmetry in the non-auroral latitudes: dawn presented densities of 1.10×10^8 m^{-3}, with a particular enhancement between 1,500 and 1,900 km, while dusk showed median densities of 5.04×10^7 m^{-3} up to 2,000 km. This observation appears counterintuitive for a molecular ion like H_3^+, which is typically expected to peak at noon under photoionization-driven conditions. However, this discrepancy does not in itself imply a new physical mechanism, as such asymmetries can still arise due to photoionization. Due to a lack of global circulation models of the upper atmosphere at low latitudes, we are unable to state exactly what is causing the observed density asymmetry. However, by comparing this work to electron profiles obtained during Juno's ROX with additional vertical profiles obtained by ground-based telescopes on the same date, it will be possible to gather more information on ionospheric layers and electron-ion dynamics.

Appendix A: List of Observations Available

Table A1.

Table A1
List of Observations From JWST Programme #3665 Taken Between 2023 and 09-07 and 2023-09-08

Observation	Latitude	Sys III longitude	UT	Local time (hr)
DAWN	35°N	151°W	10:45	06:30
DAWN	45°N	143°W	12:18	06:00
DAWN	55°N	158°W	12:51	06:00
DAWN	65°N	176°W	13:25	06:00
DAWN	75°N	181°W	14:07	05:30
DAWN	85°N	175°W	14:38	06:00
DUSK	85°N	166°W	15:09	17:30
DUSK	75°N	160°W	15:40	19:30
DUSK	15°N	33°W	22:45	19:00
DUSK	05°N	60°W	23:30	18:30
DUSK	05°S	80°W	00:15	18:30
DUSK	15°S	101°W	00:47	18:30
DUSK	25°S	125°W	01:18	18:30
DUSK	35°S	147°W	01:52	18:30
DUSK	45°S	170°W	02:23	18:00
DUSK	55°S	195°W	02:54	18:00
DUSK	65°S	225°W	03:25	18:00
DUSK	75°S	258°W	03:58	17:30
DUSK	85°S	296°W	04:29	15:30
DAWN	85°S	340°W	05:00	09:30
DAWN	75°S	25°W	05:42	07:30
DAWN	65°S	64°W	06:24	07:00
DAWN	55°S	98°W	07:05	07:00
DAWN	45°S	130°W	07:47	07:00
DAWN	35°S	160°W	08:28	07:00
DAWN	25°S	188°W	09:09	06:30
DAWN	15°S	215°W	09:50	06:30
DAWN	05°S	240°W	10:31	06:30

Table A1
Continued

Observation	Latitude	Sys III longitude	UT	Local time (hr)
DAWN	05°N	268°W	11:12	06:30
DAWN	15°N	303°W	11:57	06:30
DAWN	25°N	337°W	12:55	06:30
DUSK*	55°N	292°W	00:17	17:30
DUSK*	65°N	320°W	01:11	18:00
DUSK**	45°N	135°W	15:41	17:00
DUSK***	35°N	205°W	06:54	17:00
DUSK***	25°N	220°W	07:35	17:00

Note. The ones marked by * were recovered on 2023-12-21, the ones with ** on 2024-01-24 and the ones with *** on 2024-01-31. We indicate planetocentric latitude, System III longitude, UT of the observations and local time at limb.

Data Availability Statement

JWST data are publicly available in a raw FITS format: https://doi.org/10.17909/vjrd-5x14 (Melin & Tiranti, 2025). *h3ppy* fitting model is an open-source fitting procedure (Melin, 2025) producing H_3^+ temperatures, densities and radiances, available in the Python programming language at https://pypi.org/project/h3ppy/. Results are stored in a .h5 file with all fitted values as function of latitude, local-time, longitude and altitude, along with corresponding uncertainties, all available on Zenodo: https://doi.org/10.5281/zenodo.15188847 (Tiranti, 2025).

Acknowledgments
This work is based on observations with the NASA/ESA/CSA James Webb Space Telescope obtained from the Mikulski Archive at the Space Telescope Science Institute, which is operated by the Association of Universities for Research in Astronomy, Incorporated, under NASA contract NAS5-03127. P.I.T. was funded by UK Science and Technology Facilities Council (STFC) Studentship ST/X508548/2. H.M. was supported by the STFC James Webb Fellowship (ST/W001527/2) at Northumbria University, UK. Support for LM under Program number JWST-GO-03665.002-A was provided through a grant from the STScI under NASA contract NAS5- 03127. K.L.K. was supported by a Northumbria University Research Studentship. T.S.S. and E.M.T. were supported by an STFC Consolidated Grant (ST/W00089X/1) at Northumbria University, UK. J.O.D. was supported by the STFC Ernest Rutherford Fellowship (ST/X003426/1) at the University of Reading, UK. K.R was supported by NASA FINESST Grant 80NSSC23K1637. We acknowledge the contribution of the International Space Sciences Institute (ISSI) in Bern, Switzerland, for hosting and funding International Team 23-592 ("Jupiter's Non-Auroral Ionosphere"), and the constructive discussions by colleagues attending that meeting.

References

Achilleos, N., Miller, S., Tennyson, J., Aylward, A., Mueller-Wodarg, I., & Rees, D. (1998). Jim: A time-dependent, three-dimensional model of Jupiter's thermosphere and ionosphere. *Journal of Geophysical Research*, *103*(E9), 20089–20112. https://doi.org/10.1029/98je00947

Badman, S. V., Branduardi-Raymont, G., Galand, M., Hess, S. L., Krupp, N., Lamy, L., et al. (2015). Auroral processes at the giant planets: Energy deposition, emission mechanisms, morphology and spectra. *Space Science Reviews*, *187*, 99–179. https://doi.org/10.1007/978-1-4939-3395-2_5

Barrow, D., & Matcheva, K. I. (2011). Impact of atmospheric gravity waves on the Jovian ionosphere. *Icarus*, *211*(1), 609–622. https://doi.org/10.1016/j.icarus.2010.10.017

Barrow, D., Matcheva, K. I., & Drossart, P. (2012). Prospects for observing atmospheric gravity waves in Jupiter's thermosphere using H_3^+ emission. *Icarus*, *219*(1), 77–85. https://doi.org/10.1016/j.icarus.2012.02.007

Bougher, S., Waite Jr, J., Majeed, T., & Gladstone, G. R. (2005). Jupiter thermospheric general circulation model (JTGCM): Global structure and dynamics driven by auroral and joule heating. *Journal of Geophysical Research*, *110*(E4), E04008. https://doi.org/10.1029/2003je002230

Brown, Z., Koskinen, T., Müller-Wodarg, I., West, R., Jouchoux, A., & Esposito, L. (2020). A pole-to-pole pressure–temperature map of Saturn's thermosphere from Cassini grand finale data. *Nature Astronomy*, *4*(9), 872–879. https://doi.org/10.1038/s41550-020-1060-0

Coffin, D. A., Withers, P., Agiwal, O., Buccino, D., Parisi, M., Caruso, R. S., et al. (2025). Juno-derived electron density profiles of the high-latitude Jovian ionosphere. *Journal of Geophysical Research: Space Physics*, *130*(6), e2025JA033754. https://doi.org/10.1029/2025ja033754

Connerney, J., Timmins, S., Herceg, M., & Joergensen, J. (2020). A Jovian magnetodisc model for the Juno era. *Journal of Geophysical Research: Space Physics*, *125*(10), e2020JA028138. https://doi.org/10.1029/2020ja028138

Denneulin, L., Guilbert-Lepoutre, A., Langlois, M., Thiébaut, E., Holler, B., Ferruit, P., et al. (2023). An improved spectral extraction method for JWST/NIRSPEC fixed slit observations. *Astronomy & Astrophysics*, *679*, A63. https://doi.org/10.1051/0004-6361/202346998

Dinelli, B., Adriani, A., Mura, A., Altieri, F., Migliorini, A., & Moriconi, M. (2019). Juno/Jiram's view of Jupiter's H_3^+ emissions. *Philosophical Transactions of the Royal Society A*, *377*(2154), 20180406. https://doi.org/10.1098/rsta.2018.0406

Drossart, P., Maillard, J.-P., Caldwell, J., Kim, S., Watson, J., Majewski, W., et al. (1989). Detection of H_3^+ on Jupiter. *Nature*, *340*(6234), 539–541. https://doi.org/10.1038/340539a0

Geballe, T., Jagod, M.-F., & Oka, T. (1993). Detection of $H_3^{(+)}$ infrared emission lines in Saturn. *The Astrophysical Journal*, *408*, L109–L112. https://doi.org/10.1086/186843

Gérard, J.-C., Gkouvelis, L., Bonfond, B., Gladstone, G., Mura, A., Adriani, A., et al. (2023). H_3^+ cooling in the Jovian aurora: Juno remote sensing observations and modeling. *Icarus*, *389*, 115261. https://doi.org/10.1016/j.icarus.2022.115261

Gérard, J.-C., Gustin, J., Grodent, D., Delamere, P., & Clarke, J. (2002). Excitation of the FUV Io tail on Jupiter: Characterization of the electron precipitation. *Journal of Geophysical Research*, *107*(A11), SMP–30. https://doi.org/10.1029/2002ja009410

Grodent, D., Waite Jr, J. H., & Gérard, J.-C. (2001). A self-consistent model of the Jovian auroral thermal structure. *Journal of Geophysical Research*, *106*(A7), 12933–12952. https://doi.org/10.1029/2000ja900129

Gröller, H., Montmessin, F., Yelle, R., Lefèvre, F., Forget, F., Schneider, N., et al. (2018). MAVEN/IUVS stellar occultation measurements of Mars atmospheric structure and composition. *Journal of Geophysical Research: Planets*, *123*(6), 1449–1483. https://doi.org/10.1029/2017je005466

Gustin, J., Gérard, J.-C., Grodent, D., Cowley, S., Clarke, J., & Grard, A. (2004). Energy-flux relationship in the FUV Jovian aurora deduced from HST-STIS spectral observations. *Journal of Geophysical Research*, *109*(A10), A10205. https://doi.org/10.1029/2003ja010365

Jakobsen, P., Ferruit, P., Alves de Oliveira, C., Arribas, S., Bagnasco, G., Barho, R., et al. (2022). The near-infrared spectrograph (NIRSpec) on the James webb space telescope. I. Overview of the instrument and its capabilities. *Astronomy & Astrophysics*, *661*, A80. https://doi.org/10.1051/0004-6361/202142663

Johnson, R., Melin, H., Stallard, T. S., Tao, C., Nichols, J., & Chowdhury, M. (2018). Mapping H_3^+ temperatures in Jupiter's northern auroral ionosphere using VLT-CRIRES. *Journal of Geophysical Research: Space Physics*, *123*(7), 5990–6008. https://doi.org/10.1029/2018ja025511

Kedziora-Chudczer, L., Cotton, D., Kedziora, D., & Bailey, J. (2017). The 2μm spectrum of the auroral emission in the polar regions of Jupiter. *Icarus*, *294*, 156–171. https://doi.org/10.1016/j.icarus.2017.04.029

Knowles, K., Stallard, T., O'Donoghue, J., Moore, L., Agiwal, O., Melin, H., et al. (2025). Magnetic silhouettes in Jupiter's non-auroral ionosphere. *Journal of Geophysical Research: Space Physics*, *130*(5), e2025JA033868. https://doi.org/10.1029/2025ja033868

Koskinen, T., Sandel, B., Yelle, R., Strobel, D., Müller-Wodarg, I., & Erwin, J. (2015). Saturn's variable thermosphere from Cassini/UVIS occultations. *Icarus*, *260*, 174–189. https://doi.org/10.1016/j.icarus.2015.07.008

Koskinen, T., Yelle, R., Snowden, D., Lavvas, P., Sandel, B., Capalbo, F., et al. (2011). The mesosphere and lower thermosphere of Titan revealed by Cassini/UVIS stellar occultations. *Icarus*, *216*(2), 507–534. https://doi.org/10.1016/j.icarus.2011.09.022

Kurth, W. S., Faden, J. B., Waite, J. H., Sulaiman, A. H., Elliott, S. S., Hospodarsky, G. B., et al. (2025). Electron densities in Jupiter's upper ionosphere inferred from Juno plasma wave observations. *Journal of Geophysical Research: Planets*, *130*(3), 2024JE008845. https://doi.org/10.1029/2024JE008845

Kurth, W. S., Mauk, B. H., Elliott, S. S., Gurnett, D. A., Hospodarsky, G. B., Santolik, O., et al. (2018). Whistler mode waves associated with broadband auroral electron precipitation at Jupiter. *Geophysical Research Letters*, *45*(18), 9372–9379. https://doi.org/10.1029/2018GL078566

Lam, H. A., Achilleos, N., Miller, S., Tennyson, J., Trafton, L. M., Geballe, T. R., & Ballester, G. E. (1997). A baseline spectroscopic study of the infrared auroras of Jupiter. *Icarus*, *127*(2), 379–393. https://doi.org/10.1006/icar.1997.5698

Lystrup, M., Miller, S., Russo, N. D., Vervack Jr, R., & Stallard, T. (2008). First vertical ion density profile in Jupiter's auroral atmosphere: Direct observations using the keck ii telescope. *The Astrophysical Journal*, *677*(1), 790–797. https://doi.org/10.1086/529509

Majeed, T., Waite, J., Bougher, S., & Gladstone, G. (2009). Processes of auroral thermal structure at Jupiter: Analysis of multispectral temperature observations with the Jupiter thermosphere general circulation model. *Journal of Geophysical Research*, *114*(E7), E07005. https://doi.org/10.1029/2008je003194

Matcheva, K. I., & Strobel, D. F. (1999). Heating of Jupiter's thermosphere by dissipation of gravity waves due to molecular viscosity and heat conduction. *Icarus*, *140*(2), 328–340. https://doi.org/10.1006/icar.1999.6151

Matcheva, K. I., Strobel, D. F., & Flasar, F. (2001). Interaction of gravity waves with ionospheric plasma: Implications for Jupiter's ionosphere. *Icarus*, *152*(2), 347–365. https://doi.org/10.1006/icar.2001.6631

Mauk, B. H., Clark, G., Gladstone, G. R., Kotsiaros, S., Adriani, A., Allegrini, F., et al. (2020). Energetic particles and acceleration regions over Jupiter's polar cap and main aurora: A broad overview. *Journal of Geophysical Research: Space Physics*, *125*(3), e2019JA027699. https://doi.org/10.1029/2019ja027699

Melin, H. (2025). h3ppy: An open-source python package for modelling and fitting H_3^+ spectra. *Journal of Open Source Software*, *10*(107), 7536. https://doi.org/10.21105/joss.07536

Melin, H., Miller, S., Stallard, T., & Grodent, D. (2005). Non-LTE effects on H_3^+ emission in the Jovian upper atmosphere. *Icarus*, *178*(1), 97–103. https://doi.org/10.1016/j.icarus.2005.04.016

Melin, H., Miller, S., Stallard, T., Smith, C., & Grodent, D. (2006). Estimated energy balance in the Jovian upper atmosphere during an auroral heating event. *Icarus*, *181*(1), 256–265. https://doi.org/10.1016/j.icarus.2005.11.004

Melin, H., Moore, L., Fletcher, L. N., Hammel, H. B., O'Donoghue, J., Stallard, T. S., et al. (2025). Discovery of and infrared aurorae at Neptune with JWST. *Nature Astronomy*, *9*(5), 666–671. https://doi.org/10.1038/s41550-025-02507-9

Melin, H., O'Donoghue, J., Moore, L., Stallard, T., Fletcher, L., Roman, M., et al. (2024). Ionospheric irregularities at Jupiter observed by JWST. *Nature Astronomy*, 1–8.

Melin, H., & Tiranti, P. (2025). Data for Tiranti et al. (2025) [Dataset]. *STScI/MAST*. https://doi.org/10.17909/VJRD-5X14

Mendillo, M., Narvaez, C., Moore, L., & Withers, P. (2022). Jupiter's enigmatic ionosphere: Electron density profiles from the pioneer, voyager, and Galileo radio occultation experiments. *Journal of Geophysical Research: Planets*, *127*(3), e2021JE007169. https://doi.org/10.1029/2021je007169

Migliorini, A., Dinelli, B., Castagnoli, C., Moriconi, M., Altieri, F., Atreya, S., et al. (2023). First observations of CH_4 and spatially resolved emission layers at Jupiter equator, as seen by Jiram/Juno. *Journal of Geophysical Research: Planets*, *128*(3), e2022JE007509. https://doi.org/10.1029/2022je007509

Migliorini, A., Dinelli, B., Moriconi, M., Altieri, F., Adriani, A., Mura, A., et al. (2019). H_3^+ characteristics in the Jupiter atmosphere as observed at limb with Juno/Jiram. *Icarus*, *329*, 132–139. https://doi.org/10.1016/j.icarus.2019.04.003

Miller, S., Stallard, T., Smith, C., Millward, G., Melin, H., Lystrup, M., & Aylward, A. (2006). H_3^+: The driver of giant-planet atmospheres. *Philosophical Transactions of the Royal Society of London - A*, *364*(1848), 3121–3137. https://doi.org/10.1098/rsta.2006.1877

Miller, S., Stallard, T., Tennyson, J., & Melin, H. (2013). Cooling by H_3^+ emission. *The Journal of Physical Chemistry A*, *117*(39), 9770–9777. https://doi.org/10.1021/jp312468b

Miller, S., Tennyson, J., Geballe, T. R., & Stallard, T. (2020). Thirty years of H_3^+ astronomy. *Reviews of Modern Physics*, *92*(3), 035003.

Moore, L., Melin, H., O'Donoghue, J., Stallard, T., Moses, J., Galand, M., et al. (2019). Modelling H_3^+ in planetary atmospheres: Effects of vertical gradients on observed quantities. *Philosophical Transactions of the Royal Society A*, *377*(2154), 20190067. https://doi.org/10.1098/rsta.2019.0067

Moore, L., Nagy, A. F., Kliore, A. J., Müller-Wodarg, I., Richardson, J. D., & Mendillo, M. (2006). Cassini radio occultations of Saturn's ionosphere: Model comparisons using a constant water flux. *Geophysical Research Letters*, *33*(22), L22202. https://doi.org/10.1029/2006GL027375

Nichols, J., Badman, S. V., Bagenal, F., Bolton, S., Bonfond, B., Bunce, E., et al. (2017). Response of Jupiter's auroras to conditions in the interplanetary medium as measured by the Hubble space telescope and Juno. *Geophysical Research Letters*, *44*(15), 7643–7652. https://doi.org/10.1002/2017gl073029

Nichols, J., Clarke, J., Gérard, J.-C., Grodent, D., & Hansen, K. (2009). Variation of different components of Jupiter's auroral emission. *Journal of Geophysical Research*, *114*(A6), A06210. https://doi.org/10.1029/2009ja014051

Nichols, J., King, O., Clarke, J., de Pater, I., Fletcher, L., Melin, H., et al. (2025). Dynamic infrared aurora on Jupiter. *Nature Communications*, *16*(1), 3907. https://doi.org/10.1038/s41467-025-58984-z

O'Donoghue, J., Moore, L., Bhakyapaibul, T., Melin, H., Stallard, T., Connerney, J., & Tao, C. (2021). Global upper-atmospheric heating on Jupiter by the polar aurorae. *Nature*, *596*(7870), 54–57. https://doi.org/10.1038/s41586-021-03706-w

O'Donoghue, J., Moore, L., Stallard, T. S., & Melin, H. (2016). Heating of Jupiter's upper atmosphere above the great red spot. *Nature*, *536*(7615), 190–192. https://doi.org/10.1038/nature18940

O'Donoghue, J., & Stallard, T. (2022). What the upper atmospheres of giant planets reveal. *Remote Sensing*, *14*(24), 6326. https://doi.org/10.3390/rs14246326

Perrin, M. D., Sivaramakrishnan, A., Lajoie, C.-P., Elliott, E., Pueyo, L., Ravindranath, S., & Albert, L. (2014). Updated point spread function simulations for JWST with WebbPSF. In J. M. OschmannJr., M. Clampin, G. G. Fazio, & H. A. MacEwen (Eds.), *Space telescopes and instrumentation 2014: Optical, infrared, and millimeter wave* (Vol. 9143, p. 91433X). https://doi.org/10.1117/12.2056689

Quémerais, E., Bertaux, J.-L., Korablev, O., Dimarellis, E., Cot, C., Sandel, B. R., & Fussen, D. (2006). Stellar occultations observed by spicam on Mars express. *Journal of Geophysical Research*, *111*(E9), E09S04. https://doi.org/10.1029/2005je002604

Rishbeth, H. (1988). Basic physics of the ionosphere: A tutorial review. *Journal of the Institution of Electronic and Radio Engineers*, *58*(6S), S207–S223. https://doi.org/10.1049/jiere.1988.0060

Roberts, K., Moore, L., O'Donoghue, J., Melin, H., Stallard, T., Knowles, K. L., et al. (2025). Spatiotemporal variations of temperature in Jupiter's upper atmosphere. *The Planetary Science Journal*, *6*(4), 92. https://doi.org/10.3847/psj/adc09b

Smith, C., & Aylward, A. (2009). Coupled rotational dynamics of Jupiter's thermosphere and magnetosphere. *Annales Geophysicae*, *27*(1), 199–230. https://doi.org/10.5194/angeo-27-199-2009

Sromovsky, L. A., & Fry, P. M. (2010). The source of widespread 3-μm absorption in Jupiter's clouds: Constraints from 2000 Cassini VIMS observations. *Icarus*, *210*(1), 230–257. https://doi.org/10.1016/j.icarus.2010.06.039

Stallard, T. S., Burrell, A. G., Melin, H., Fletcher, L. N., Miller, S., Moore, L., et al. (2018). Identification of Jupiter's magnetic equator through H_3^+ ionospheric emission. *Nature Astronomy*, *2*(10), 773–777. https://doi.org/10.1038/s41550-018-0523-z

Stallard, T. S., Melin, H., Miller, S., Badman, S. V., Baines, K. H., Brown, R. H., et al. (2015). Cassini vims observations of H_3^+ emission on the nightside of Jupiter. *Journal of Geophysical Research: Space Physics*, *120*(8), 6948–6973. https://doi.org/10.1002/2015ja021097

Sulaiman, A., Mauk, B., Szalay, J., Allegrini, F., Clark, G., Gladstone, G., et al. (2022). Jupiter's low-altitude auroral zones: Fields, particles, plasma waves, and density depletions. *Journal of Geophysical Research: Space Physics*, *127*(8), e2022JA030334. https://doi.org/10.1029/2022ja030334

Tao, C., Badman, S. V., & Fujimoto, M. (2011). UV and IR auroral emission model for the outer planets: Jupiter and Saturn comparison. *Icarus*, *213*(2), 581–592. https://doi.org/10.1016/j.icarus.2011.04.001

Tikhonov, A., & Arsenin, V. Y. (1977). *Solutions of ill-posed problems*. VH Winston & Sons, a division of Scripta Technica. Inc.

Tiranti, P. (2025). Jupiter vertical profile JWST #3665 [Dataset]. *Zenodo*. https://doi.org/10.5281/ZENODO.15188847

Trafton, L., Geballe, T., Miller, S., Tennyson, J., & Ballester, G. (1993). Detection of $H_3^{(+)}$ from Uranus. *Astrophysical Journal Part 1*, *405*(2), 761–766. https://doi.org/10.1086/172404

Uno, T., Kasaba, Y., Tao, C., Sakanoi, T., Kagitani, M., Fujisawa, S., et al. (2014). Vertical emissivity profiles of Jupiter's northern H_3^+ and H_2 infrared auroras observed by Subaru/IRCS. *Journal of Geophysical Research: Space Physics*, *119*(12), 10–219. https://doi.org/10.1002/2014ja020454

Valek, P., Allegrini, F., Bagenal, F., Bolton, S., Connerney, J., Ebert, R., et al. (2019). Jovian high-latitude ionospheric ions: Juno in situ observations. *Geophysical Research Letters*, *46*(15), 8663–8670. https://doi.org/10.1029/2019gl084146

Waite, J., Jr., Cravens, T., Kozyra, J., Nagy, A., Atreya, S., & Chen, R. (1983). Electron precipitation and related aeronomy of the Jovian thermosphere and ionosphere. *Journal of Geophysical Research*, *88*(A8), 6143–6163. https://doi.org/10.1029/ja088ia08p06143

Walsh, A. P., Haaland, S., Forsyth, C., Keesee, A. M., Kissinger, J., Li, K., et al. (2014). Dawn–dusk asymmetries in the coupled solar wind–magnetosphere–ionosphere system: A review. *Annales Geophysicae*, *32*(7), 705–737. https://doi.org/10.5194/angeo-32-705-2014

Wilson, R., Vogt, M., Provan, G., Kamran, A., James, M., Brennan, M., & Cowley, S. (2023). Internal and external Jovian magnetic fields: Community code to serve the magnetospheres of the outer planets community. *Space Science Reviews*, *219*(1), 15. https://doi.org/10.1007/s11214-023-00961-3

Yates, J., Ray, L. C., Achilleos, N., Witasse, O., & Altobelli, N. (2020). Magnetosphere-ionosphere-thermosphere coupling at Jupiter using a three-dimensional atmospheric general circulation model. *Journal of Geophysical Research: Space Physics*, *125*(1), e2019JA026792. https://doi.org/10.1029/2019ja026792

Yelle, R. V., & Miller, S. (2004). Jupiter's thermosphere and ionosphere. *Jupiter: The Planet, Satellites and Magnetosphere*, *1*, 185–218.

Young, L. A., Yelle, R. V., Young, R., Seiff, A., & Kirk, D. B. (1997). Gravity waves in Jupiter's thermosphere. *Science*, *276*(5309), 108–111. https://doi.org/10.1126/science.276.5309.108